POLITECNICO DI TORINO
Repository ISTITUZIONALE

Robocasting of single and multi-functional calcium phosphate scaffolds and its hybridization with conventional techniques: Design, fabrication and characterization

(Article begins on next page)

16 July 2022

Robocasting of Single and Multi-Functional Calcium Phosphate Scaffolds and Its Hybridization with Conventional Techniques: Design, Fabrication and Characterization

Mehdi Mohammadi [1,*], Patricia Pascaud-Mathieu [2], Valeria Allizond [3,*], Jean-Marc Tulliani [1], Bartolomeo Coppola [1], Giuliana Banche [3], Christophe Chaput [4], Anna Maria Cuffini [3], Fabrice Rossignol [2] and Paola Palmero [1]

1   Department of Applied Science and Technology, INSTM R.U. Lince Laboratory, Politecnico di Torino, Corso Duca degli Abruzzi, 24, 10129 Turin, Italy; jeanmarc.tulliani@polito.it (J.-M.T.); bartolomeo.coppola@polito.it (B.C.); paola.palmero@polito.it (P.P.)
2   IRCER, UMR CNRS 7315, University of Limoges, F-87000 Limoges, France; patricia.pascaud-mathieu@unilim.fr (P.P.-M.); fabrice.rossignol@unilim.fr (F.R.)
3   Bacteriology and Mycology Laboratory, Department of Public Health and Pediatrics, University of Torino, Via Santena 9, 10126 Turin, Italy; giuliana.banche@unito.it (G.B.); annamaria.cuffini@unito.it (A.M.C.)
4   3D-Ceram Company (Sinto Group), 27 Rue du Petit Theil, 87280 Limoges, France; christophe.chaput@3dceram.com
*   Correspondence: mehdi.mohammadi@polito.it (M.M.); valeria.allizond@unito.it (V.A.); Tel.: +39-011-0904678 (M.M.); +39-011-6705644 (V.A.)

Featured Application: Hard tissue repair and replacement including large and small scales injuries with tailored mechanical and biological properties, featured by controlled local drug delivery systems to prevent post-surgical infection, to improve tissue regeneration, and/or for anticancer activities.

Abstract: In this work, dense, porous, and, for the first time, functionally-graded bi-layer scaffolds with a cylindrical geometry were produced from a commercially available hydroxyapatite powder using the robocasting technique. The bi-layer scaffolds were made of a dense core part attached to a surrounding porous part. Subsequently, these bi-layer robocast scaffolds were joined with an outer shell of an antibacterial porous polymer layer fabricated by solvent casting/salt leaching techniques, leading to hybrid ceramic-polymer scaffolds. The antibacterial functionality was achieved through the addition of silver ions to the polymer layer. All the robocast samples, including the bi-layer ones, were first characterized through scanning electron microscopy observations, mechanical characterization in compression and preliminary bioactivity tests. Then, the hybrid bi-layer ceramic-polymer scaffolds were characterized through antimicrobial tests. After sintering at 1300 °C for 3 h, the compressive strengths of the structures were found to be equal to 29 ± 4 MPa for dense samples and 7 ± 4 MPa for lattice structures with a porosity of 34.1%. Bioactivity tests performed at 37 °C for 4 weeks showed that the precipitated layer on the robocast samples contained octacalcium phosphate. Finally, it was evidenced that the hybrid structure was effective in releasing antibacterial Ag^+ ions to the surrounding medium showing its potential efficiency in limiting *Staphylococcus aureus* proliferation during surgery.

Keywords: additive manufacturing; robocasting; hybrid technologies; calcium phosphates; scaffold; functionally-graded materials; hybrid ceramic-polymer scaffold; polycaprolactone; osteoconductivity; anti-staphylococcal properties

1. Introduction

Tissue engineering is an alternative to bone grafting procedures, which aims to integrate engineering and life science criteria to develop reliable and physiologically acceptable solutions for bone regeneration [1]. From the tissue engineering point of view, an ideal bone graft must meet strict requirements regarding its biological, physical and mechanical characteristics. An ideal bone graft must be osteoconductive and osteoinductive and also gradually be degraded in the body fluid providing adequate space for the new bone to grow [2,3]. Such biological properties can be provided using calcium phosphate (CaP) bioceramics in the form of highly porous scaffolds with suitable architecture [4]. The scaffolds must fulfill special physical characteristics regarding porosity level, and pore and interpore channel sizes to supply proper cell attachment and vascularization [1,5–9]. Besides, surface topography, as well as surface charge and crystallinity, are also claimed to play key roles in guiding protein adsorption and consequently cell adhesion [10]. An ideal bone graft must also possess enough mechanical strength to structurally support the newly formed tissue. However, high mechanical properties are generally in contrast with the high biological performance of an implant [11]. In other words, improved biological properties of highly porous structures take place along with a decrease in their mechanical integrity [12,13].

One solution to accomplish such contradictory properties is to design the scaffold as a functionally graded structure (FGM) made from layers with different porosity levels. FGMs are defined as structures that show compositional or microstructural transition along with at least one direction designed to fulfill two or more functions simultaneously [14]. Natural bone is an example of a FGM structure in which the variation of the pore sizes and distributions across the transverse section provides a graded body. The fabrication of artificial bone grafts can be inspired from this morphological variation and be designed in multi-layer structures composed of different porous and dense layers, to fulfill both biological and mechanical requirements. Production of FGM structures from CaP bioceramics has been reported in several works where the FGM structures were produced in two [15–18] or more layers [19], with improved mechanical and biological properties compared to single-layer materials. However, in all cases, the structures were produced using conventional ceramic processing methods such as freeze casting [15,16,18,20], pressing [17] and gelcasting [21,22] with limited control on the scaffold architecture [14].

An alternative to conventional ceramic processing methods is additive manufacturing (AM). AM is a novel manufacturing method that is inherently suitable for the production of complex parts like biomedical scaffolds. Contrary to conventional methods, AM makes it possible to precisely control the scaffold architecture, pore size and pore network [14]. Robocasting is an AM technique particularly suitable for the fabrication of ceramic parts in which the feed material is a highly concentrated ceramic paste. The paste is deposited continuously through a nozzle in the form of filaments and the whole part is fabricated from these filaments [23]. A robotic arm controls the displacement of the nozzle in accordance with a computer-aided design (CAD) model. Production of complex structures from different ceramics such as alumina [24–26], silicon carbide [27,28], bioglasses [29–31], and electroceramics [32] has been reported in the literature. Due to the high green density, high fired densities and therefore high mechanical properties can be achieved after sintering [33,34].

Production of CaP structures by robocasting technique was also reported in several papers. These studies range from the fabrication of simple geometries to customized complex structures designed based on the individual patient's data [35–41]. However, most of the studies were focused on the demonstration of the suitability of the formulated paste for the fabrication of porous structures representing different final porosities and pores sizes [35,36,38,41]. While attempts have also been conducted to increase the mechanical properties of the printed scaffolds through soaking the produced structures in the simulated body fluid (SBF) [36,42] or polymer infiltration [37,39,43], no studies have been reported on the production of dense or FGM CaP structures through this technique.

The last concern relates to probable inflammation and infection in the surgery site, due to bacterial adhesion to the implant surface. Generally, bacterial adhesion originates from the surgery and escapes from immunological surveillance [44]. It is shielded from the host immune system by the

formation of bacterial biofilms making any antibiotic therapy ineffective. This circumstance leads to implant loss and inevitable revised surgery [44,45]. The most reliable way to avoid bacterial adhesion is the incorporation of antibacterial agents such as silver, copper, zinc, mercury, tin, etc. into/onto implants [44,46]. Among these elements, silver has been exploited since ancient times as an effective antimicrobial agent that inhibits bacterial replications by damaging their RNA and DNA [47]. In comparison with other heavy metals, silver also shows remarkably low toxicity [45].

This paper is divided into two parts. In the first (main) part, the production of porous, dense and bi-layer scaffolds using the robocasting technique from a commercially available hydroxyapatite (HA) powder is reported. The fabrication of a bi-layer robocast sample in a single printing step is a key innovation, as no previous examples—to the best of the authors' knowledge—are currently available in the literature. The bi-layer scaffolds were made of a dense core part designed to provide load-bearing function, and a surrounding porous part to provide biological performances. Physical, mechanical and bioactivity properties of the new scaffolds were characterized. The biodegradation properties of the scaffolds were already verified in the authors' previous work by in vitro dissolution tests, by immersion of the samples in a 0.1M tris(hydroxymethyl) aminomethane solution, at physiological pH and 37 °C, up to 17 days [21]. The second part is dealing with the hybridization of the robocasting technique with conventional routes for the processing of polymer parts, with the aim to provide further functionalities to the scaffolds. Such an original approach implies the joining of the bi-layer robocast scaffold with an antibacterial porous polymer outer layer fabricated by solvent casting/salt leaching techniques. The antibacterial functionality was achieved through the addition of silver ions to the polymer layer and validated through antimicrobial tests. The effective release of silver ions proved the ability of the polymer layer to provide the desired functionality; however, in the future different drugs could be added as well, to respond to specific requirements.

2. Materials and Methods

2.1. Robocasting

2.1.1. Design of CAD Models

Three different types of scaffolds were designed for fabrication: lattice, dense and bi-layer FGM structures. The digital 3D models of the objects were obtained through CAD software (AutoCAD 2018, Autodesk, Inc., Mill Valley, CA, USA) as can be seen in Figure 1. The designs were then converted into stereolithography files (STL) which were subsequently sliced (Cura 3.6, Ultimaker, Geldermalsen, The Netherlands) into two-dimensional (2-D) layers in a virtual environment along with printing instructions in three different G-code files. The G-code files were translated by a 3D printing client software instructing the 3D printer to achieve computer-controlled layer-by-layer extrusion of the paste.
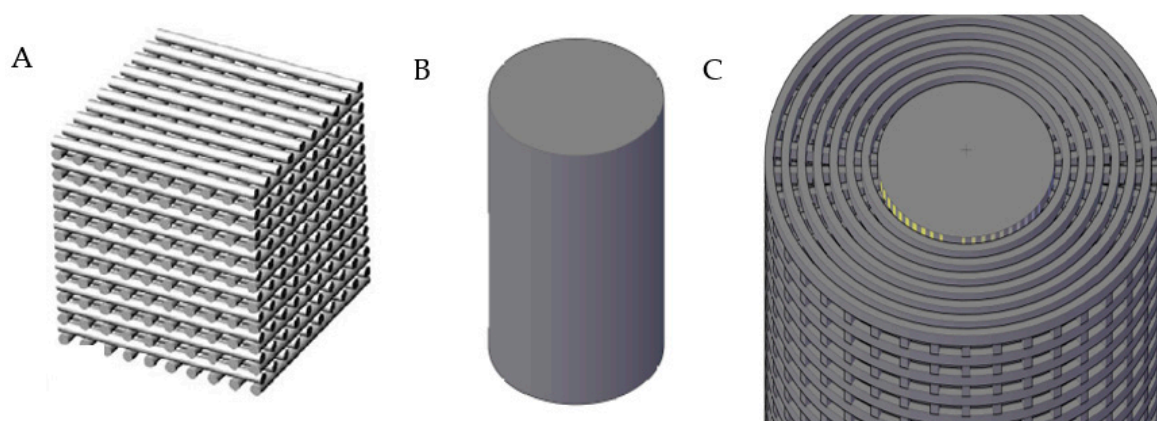
Figure 1. Schematic illustration of the 3D CAD designs for robocasting; lattice (**A**), dense (**B**) and bi-layer (**C**) models.

The lattice porous part was a network of struts comprising a tetragonal geometry with the dimensions of $9.6 \times 9.6 \times 7.3$ mm^3. It was made of parallel linear rods aligned in the *x*- and *y*-axis in such a way that subsequent layers oriented at right angles. The part consisted of 24 layers and each layer contained 12 parallel struts with a diameter of 400 µm. The parallel rods in each layer were separated equal to the struts sizes resulting in the center-to-center rod spacing of 800 µm. To provide appropriate consolidation between parallel layers and maintain the integrity of the whole part, the spacing in the *z*-axis was defined as 300 µm. As several parameters such as paste formulation, the geometry of the structure, slicing procedure and printing parameters affect the robocasting outcome, in order to focus on the paste formulation and minimize the effects of other parameters, the cubic geometry was selected for the lattice structure to have the simplest possible raster pattern consisting of parallel straight rods without any circular travels or sharp edges.

The dense part was a monolithic cylinder with a diameter of 10 mm and a height of 15 mm. With the infill of 100%, the rod spacing between the filaments was defined as equal to d/1.2, where d is the diameter of the nozzle. The rod spacing was found sufficiently small to cause the filaments to completely squeeze together during printing, but not too small to cause overfill of the area being printed [27].

The bi-layer structure was a combination of dense and lattice parts designed as an FGM structure mimicking the natural bone assembly. A radial gradient was achieved by designing the porous part around a dense cylindrical core. The porous part was composed of successive repetitions of two different layers: a layer of radial rods and another layer consisting of concentric rings with different diameters in such a way that the porosity increased from the center to the periphery. Each rod in the lattice part was composed of two adjacent 400 µm filaments printed next to each other forming struts of 800 µm thickness. The final design had a diameter of 20 mm and a height of 19.6 mm. The central dense core diameter was 8.8 mm.

2.1.2. Materials

A commercially available hydroxyapatite powder, $Ca_{10}(PO_4)_6(OH)_2$ (Captal S, batch P270S BM 192 Lot 2, Plasma Biotal, Buxton, UK) was used as the constituent phase in the pastes. Full characterizations of the powder as well as its optimum sintering condition were already published in the authors' previous paper [48]. Briefly, the powder is a calcium-deficient HA (CD-HA) with a Ca/P atomic ratio of 1.59 and a starting particle size of 2.48 µm. By wet ball milling, the average particle size was reduced to 0.74 µm [48] as measured by laser granulometry (Laser Particle Sizer Analysette 22; Fritsch, Idar-Oberstein, Germany).

For the paste preparation, Darvan C-N an ammonium polymethacrylate dispersing agent (15,000 g·mol^{-1}, Vanderbilt Minerals, LLC, Norwalk, CT, USA) was mixed with demineralized water followed by the dissolution of the required amount of hydroxypropyl methylcellulose (Methocel E4M, Dow Chemical Company, Midland, MI, USA) as a viscosifying agent. Then, ball-milled HA powder was added to the mixture in small amounts and homogenized properly after each addition. The final solid loadings of the pastes are presented in Table 1. In order to remove large agglomerates, the powder was already sieved under 80 µm. Polyethylenimine (PEI, branched, Sigma Aldrich, Darmstadt, Germany) was finally added to produce the gelation of the paste. The different paste formulations used for the fabrication of the robocast parts are reported in Table 1.

Table 1. Different paste formulations used for the fabrication of the robocast parts.

Scaffold Type	Paste Code	Solid Loading (vol%)	Dispersant (%)	Methocel (%)	PEI (%)	Printing Speed (mm/min)
	P1	49.2	4	6.5	16	290
Lattice	P2	49.2	4	3.5	8	290
	P3	51.0	4	6.5	8	290
Dense	P3	51.0	4	6.5	8	226
Bi-layer	P3	51.0	4	6.5	8	129

2.1.3. Scaffolds Fabrication

A custom-designed robotic deposition device equipped with a screw-type extruder and mounted on a Stepcraft 840 V2 CNC machine (Stoneycnc, Dublin, UK) was used for the 3D printing of the scaffolds. A computer-aided direct-write program controlled the extruder motion in 3 axes. The printing capsule was partially filled with the formulated paste, with special care to avoid trapping of air bubbles. An alumina plate was used as the substrate for the deposition of the filaments and the printings were done at room temperature. To avoid the fast drying of the deposited filaments, the relative humidity of the printing chamber was regulated over 55%.

The printed parts were dried by gradually reducing the humidity level of the chamber at room temperature over 24 h. The samples were carefully separated from the substrate to avoid any damage and submitted to debinding (up to 500 °C at 1 °C/min) and sintering (up to 1300 °C for 3 h at 5 °C/min).

2.1.4. Scaffolds Characterizations

The Archimedes' method according to ISO 10545-3:2018 [49] was used for the density and porosity measurements. The sintered densities and open porosities were determined by:

$$\rho_s = \frac{M_{dry}}{\left(M_{sat} - M_{susp}\right)} \rho_{water} \tag{1}$$

$$Open\ Porosity\ (\%) = \frac{\left(M_{sat} - M_{dry}\right)}{\left(M_{sat} - M_{susp}\right)} 100\% \tag{2}$$

where ρ_s, ρ_{water}, M_{dry}, M_{sat} and M_{susp} are the density of the scaffold being measured, the density of water at the measurement temperature, the scaffold mass, the scaffold mass being saturated by deionized water and the mass found by suspending the saturated scaffold in deionized water, respectively.

The pores and strut sizes were characterized using a stereomicroscope (Leica EZ4 W, Wetzlar, Germany). The microstructures of the samples were observed using field emission scanning electron microscopy (FESEM) (Zeiss Supra 40, Jena, Germany), equipped with an Oxford EDS microanalysis (Oxford Instrument plc, Abingdon, UK) for chemical analyses. The mechanical properties of the dense and porous samples were determined according to ASTM C773-88 (2016) [50] using a uniaxial compression testing device (MTM Zwick/Roell Z050, ZwickRoell AG, Ulm, Germany) having a 50 kN load capacity in displacement-controlled mode and with a displacement rate of 0.1 mm/min. At least 6 samples were tested from each scaffold type. Despite that ceramics can be characterized by different physical-mechanical tests [51–53], the uniaxial compression test is widely used for dense and porous bioceramics, thus providing a useful tool to compare the current results with literature previous ones.

The fracture mode of the porous samples under uniaxial compressive loading was identified by performing compression tests in an environmental scanning electron microscope (ESEM, Quanta 450 FEG, ThermoFisher Scientific, Waltham, MA, USA). While testing, loading and displacement were monitored, and at any sudden drop of loading the test was stopped and possible crackings were identified by in situ observation of the specimen.

In vitro bioactivity tests were carried out on the FGM structure by soaking the samples in simulated body fluid (SBF) solution according to ISO 23317:2014 [54]. The SBF was prepared by dissolving proper amounts of sodium chloride (NaCl), potassium chloride (KCl), sodium hydrogen carbonate (NaHCO$_3$), magnesium chloride hexahydrate (MgCl$_2$·6H$_2$O), dipotassium hydrogen phosphate trihydrate (K$_2$HPO$_4$·3H$_2$O), hydrochloric acid solution (HCl), sodium sulfate (Na$_2$SO$_4$) and calcium chloride dihydrate (CaCl$_2$·2H$_2$O) in deionized water [54]. Trishydroxymethyl aminomethane (TRIS) and 1 mol/L HCl fluid were used for buffering of the solution at pH 7.40 at 37 °C. Disc-shaped specimens were placed in transparent plastic containers with the standard configuration and the SBF solution was

added to the bottles. The following formula was used for the calculation of the required volume of the SBF solution which is a function of the apparent surface area of the specimen:

$$v_s = 100(mm) \cdot S_a \tag{3}$$

In this formula, v_s and S_a are the volume of SBF in mm^3 and the apparent surface area of the specimen in mm^2, respectively. The soaking was performed for 4 weeks at 37 °C and afterward, the samples were washed by ultrapure deionized water and were dried subsequently. SEM observations were conducted on the lower surface of the samples, as recommended by ISO 23317:2014 standard, after coating with a thin film of Pt–Pd.

2.2. Hybrid Technologies: Robocasting Joined with Polymer Processing Routes

2.2.1. Fabrication of Hybrid Ceramic-Polymer Scaffolds

An original attempt to join the ceramic robocast sample to a porous polymeric layer, able to provide new functionalities to the scaffold, was carried out. To this aim, the robocasting technology to fabricate the ceramic part was combined with a solvent casting/salt leaching technique for the fabrication of the foamed polymer. In order to demonstrate the achievement of multi functionalities of the scaffold, silver ions were added to the polymer layer to provide antimicrobial properties. The polymeric matrix was made of Poly(ε-caprolactone) (PCL, Mw 80000, Sigma Aldrich, Milan, Italy) reinforced by a 70/30 mixture of HA and β-TCP (whitlockite, batch P346S OD, Plasma Biotal, Buxton, UK) particles. The PCL to CaP mass ratio was 60:40 and Ag^+ was added as $AgNO_3$ compound, by using 1.7 wt% of $AgNO_3$ with respect to the polymer mass equal to 1 wt% of $AgNO_3$ with respect to the total mass (polymer and CaP), in accordance with previous literature [55].

$AgNO_3$ was dissolved in acetone (Sigma Aldrich, Milan, Italy) under magnetic stirring for 72 h. After the addition of the biphasic calcium phosphate (BCP) mixture, the suspension was homogenized for a further 24 h. Afterward, PCL was added and for its complete dissolution, the mixture was stirred for a further 24 h at 40 °C. Then, NaCl granules (Sigma Aldrich, Milan, Italy), sieved in the 125–355 μm range, were added to the mixture as porogen agents. After homogenization, the suspension was cast around the sintered bi-layer robocast samples which were already placed in plastic molds (30 mm diameter). Control samples were also prepared under the same procedure but without $AgNO_3$ addition.

Drying was carried out for 24 h at room temperature, to completely evaporate acetone. Porosity was achieved by the salt leaching method, by soaking the samples in deionized water to remove the salt. The samples were immersed for 4 days and the water was refreshed each 24 h.

2.2.2. In-Vitro Bacterial Adhesion Assay

The antibacterial behavior of the samples was investigated based on a quantitative bacterial adhesion assay and a sonication protocol was used to dislodge adherent bacteria. In parallel, the effect of the different biomaterials on the number of planktonic bacteria was also determined. The antiadhesive and antibacterial activities of the Ag-modified scaffolds were tested against a biofilm-producing *Staphylococcus aureus* ATCC 29,213 [56–59]. In detail, staphylococci stored at −80 °C were cultured overnight at 37 °C in Mueller Hinton Broth (MHB; Becton Dickinson and Company, Franklin Lakes, NJ, USA). After incubation, bacteria were centrifuged, and the pellet was re-suspended in 100 μL of MHB and then diluted in MHB to 10^4 CFU/mL, as confirmed by colony counts on Mueller Hinton Agar (MHA; Becton Dickinson and Company, Franklin Lakes, NJ, USA). The sterile samples were transferred into a multiwell culture plate, covered with 7 mL of staphylococcal suspension, and incubated by shaking for 24 h at 37 °C to allow in vitro bacterial adhesion. Controls represented by bacteria incubated in MHB with no material were also performed. The number of strongly bound bacteria on the scaffolds after incubation was quantified after sonication (40 kHz) for 30 min at 22 °C in 10 mL of sterile saline solution 0.9% (Bieffe Medital S.p.A., Grosotto, Italy). The number of CFU in

each sonication product was quantified by plating on MHA the pellet obtained after centrifugation. The number of planktonic bacteria (CFU/mL) was also determined. All experiments, assayed in triplicate, were performed simultaneously for each material and repeated a minimum of three times. The microbiological data, expressed as CFU/mL, were analyzed by descriptive statistics (mean values and standard error of the means) and tested by unpaired Student's t-test to highlight significant differences ($p < 0.05$) between the different biomaterials by using the GraphPad Prism 8 software (San Diego, CA, USA). Besides, in order to prove the antimicrobial properties of the Ag-modified scaffolds, the same procedure was applied to Ag-free hybrid ceramic/polymer scaffolds.

3. Results and Discussions

3.1. Robocasting of Lattice, Dense and Bi-Layer Parts

3.1.1. Paste Formulations

Table 1 presents the constituents of paste formulations used to print the three types of scaffolds. In this table, the percentage of the dispersant is calculated in relation to the solid content, and the methocel and PEI values are calculated in relation to the water content of the pastes. P1 was the first formulation that led to the successful printing of the lattice parts, at 49.2 vol% solid along with 6.5 and 16% of methocel and PEI, respectively. However, the high organic matter content in this formulation could lead to residual pores during sintering, and thus to incomplete consolidation [60]. Therefore, in order to reduce the organic matter, P2 was prepared at the same solid loading as P1 but at reduced methocel and PEI amounts (they were decreased from 6.5 to 3.5 and 16 to 8%, respectively). However, as can be seen in Figure 2, the samples made from P2 showed several surface cracks once they were dried. The problem was overcome by restoring the methocel concentration to 6.5% (P3). It seemed that at the reduced amount of methocel as a viscosifying agent, the evaporation of water took place at higher speeds inducing local drying stresses. The new formulation (P3) was prepared at a higher solid loading (51 vol%) than the previous ones (49 vol%), still showing a good printability. Therefore, this P3 formulation was selected for the printing of all structures of which the obtained results are presented hereinafter.
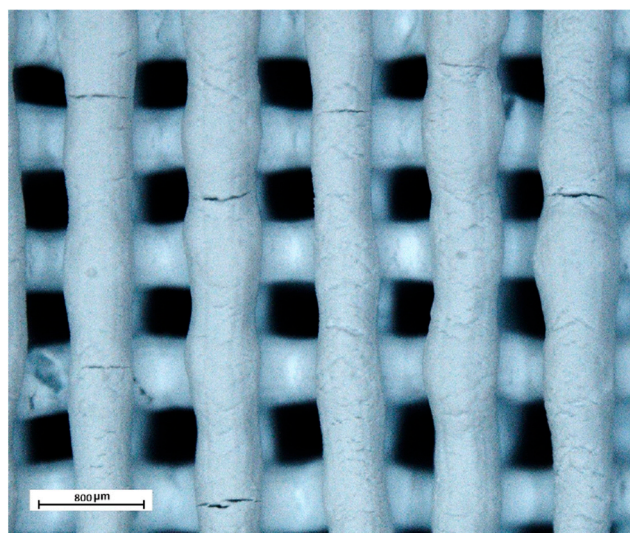
Figure 2. Stereomicroscope observation of a dried porous sample fabricated from P2 indicating drying cracks on the filaments' surfaces.

Although higher speeds are more desirable to lower the printing time, the printings of dense and especially bi-layer samples were more problematic. Because of the sharp corners and also different raster patterns containing circular travels, the printing speeds were decreased from 290 to 226 mm/min

for the dense samples and to 129 mm/min for the bi-layer samples as indicated in Table 1. In fact, at higher printing speeds, the tool paths were less accurate, and changing direction at corners reduced their sharpness to rounded edges. However, it must be considered that the printability of any structure is a function of several factors such as paste formulation and rheology, the shape of the part, the printing speed, nozzle sizes, temperature and relative humidity of the printing chamber, etc. and a successful printing is achieved when these parameters are controlled concurrently.

3.1.2. Porous Parts

Figure 3 collects some representative digital photographs of a sintered 3D lattice sample from the perspective, top and side views. It can be seen that the sample kept its regular quadratic channel structure after post-printing processing such as drying, debinding and sintering, and the structures were, in general, highly defined and precise. The struts stretched without any noticeable deformation along X and Y directions and no macro-cracks were observed. The average dimensions of the dried and sintered samples were $9.21 \times 9.21 \times 7.00$ and $7.55 \times 7.55 \times 5.75$ mm^3 respectively, indicating 4.06% and 18.02% drying and sintering shrinkages, respectively.
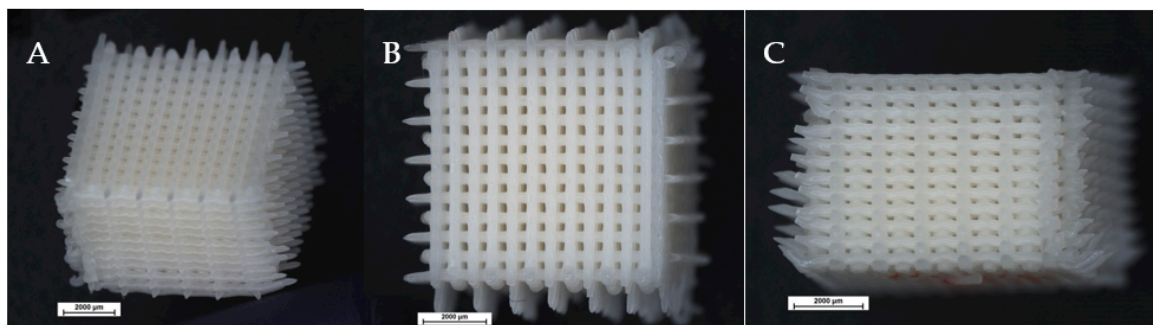
Figure 3. A representative lattice sample from different views; Perspective (**A**), top (**B**) and side (**C**) views.

In Figure 4, a scanning electron micrograph (SEM) image shows the connection of two interpenetrating struts of a lattice scaffold. The traversing filaments (T) show homogeneous microstructure without noticeable borderline between them, highlighting a very well integration between successive layers through production steps. A deeper insight into the image shows a highly compact, well-sintered microstructure, with few residual pores.
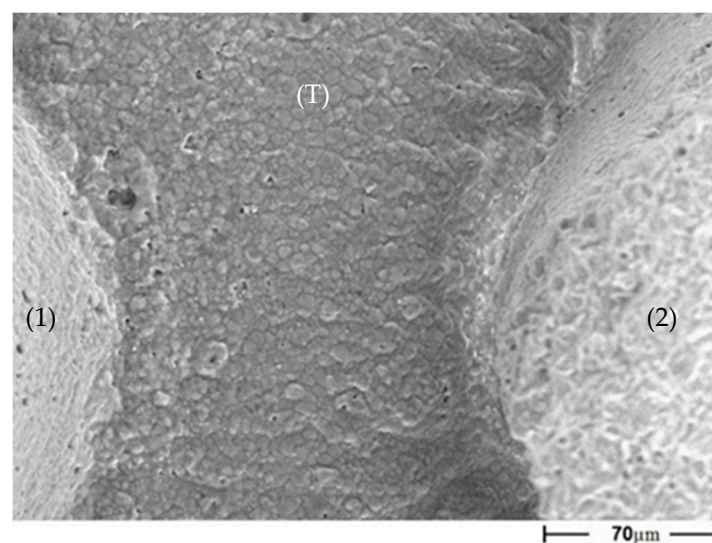
Figure 4. SEM image showing the contact area between interconnecting rods of adjacent layers.

The physical characteristics of the sintered 3D scaffolds are listed in Table 2 (as average values of at least 10 samples). The relative density of the solid was calculated considering the final composition of samples as a 70/30 mixture of HA/β-TCP, as determined in a previous paper [48] (the densities of HA and β-TCP phases were considered as 3.15 and 3.07 g/cm^3, respectively). As the optimum pore size range for bone regeneration was proposed from 100 to 400 μm [61], the lattice scaffolds with an average pore width of 275 μm can be considered suitable for biomedical applications. Moreover, the relative density of the solid parts was 95%, showing an optimum density of the struts. Therefore, it can be said that the porous samples (i) being composed of a mixture of HA and β-TCP, which considered as the optimum composition for biological activities, (ii) having interconnected pores with optimum size for bone regeneration, and (iii) having the optimum solid density of 95% (theoretical density (TD), can be considered as suitable materials for bone replacement applications from the biological point of view.

**Table 2.** Physical characteristics of different 3D structures.

Scaffold Type	Strut Size (μm)	Pore Size (μm)	Apparent Density (g/cm^3)	Density of Solid Part (g/cm^3)	Relative Density of Solid (%)	Total Porosity (%)	Open Porosity (%)
Lattice	341 ± 7	275 ± 8	2.06 ± 0.10	2.97 ± 0.01	95	34.1	30.7 ± 3.4
Dense	-	-	2.69 ± 0.20	2.95 ± 0.01	95	13.9	8.7 ± 1.6
Bi-layer	619 ± 21	605 ± 55–1040 ± 31	2.19 ± 0.10	2.99 ± 0.01	96	29.9	26.8 ± 2.6

3.1.3. Dense Parts

Representative images of the dense samples after sintering are presented in Figure 5. The dense samples were cylinders with regular structures and precise dimensions, in good agreement with the CAD design. With the average heights of 13.88 ± 0.15 and 11.67 ± 0.09 mm in the dried and sintered conditions, respectively, the samples exhibited 15.90 ± 0.05% linear shrinkage during the sintering (the values are the average of at least 10 samples). Compared to the lattice samples, they had lower sintering shrinkage, in agreement with the results published by Roopavath et al. [62] who showed that the sintering shrinkage of HA scaffolds has a reverse relationship with their infills. As listed in Table 2, density and porosity measurements provided 8.7 ± 1.6% open porosity. The density of solid in these parts was comparable to the porous parts (95%TD) but the presence of open porosities decreased the average apparent density to 2.69 g/cm^3. As can be seen in Figure 6, these open porosities stemmed from the separation of the adjacent filaments during the post-printing processes. It seems that these filaments did not squeeze well into each other during printing resulting in spaces between them in the final structure. These flaws were more pronounced at the center of the samples than in peripheries.


Figure 5. Representative dense samples, showing well-constructed cylinders with regular dimensions.
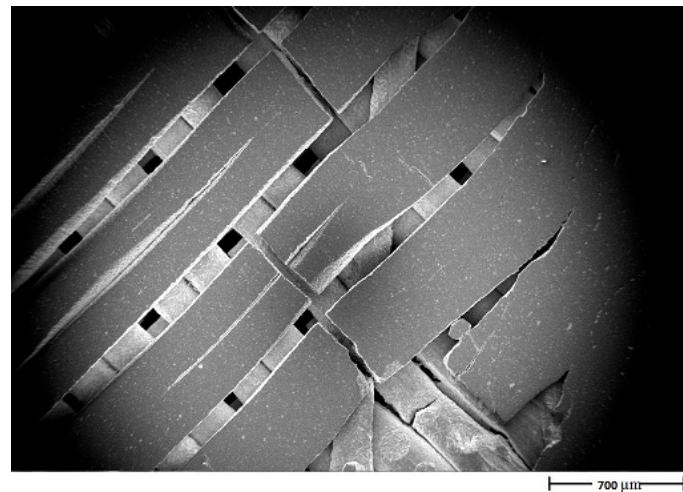
Figure 6. Low magnification SEM image of a dense sample illustrating open spaces between filaments.

3.1.4. FGM Bi-Layer Parts

Stereomicroscopy images of a representative bi-layer FGM sample from top and side views are presented in Figure 7. It can be seen that these samples were a regular combination of a dense part surrounded by four concentric rings with different diameters. The dense part and the rings were bonded together by radial filaments providing a well-suited firm structure. Open pores in the shape of isosceles trapezoids were created by the interception of the concentric rings and radial filaments of which sizes increased by distancing from the dense core. However, several detachments of the neighboring filaments in the porous section were observed. The presence of these flaws along with a similar problem in dense samples underlines the importance of considering the right amount of overlap between two adjacent rods in the slicing phase of the CAD designs, such that the rods squeeze into each other during consolidation, and the sintering shrinkage does not result in their disjunction.
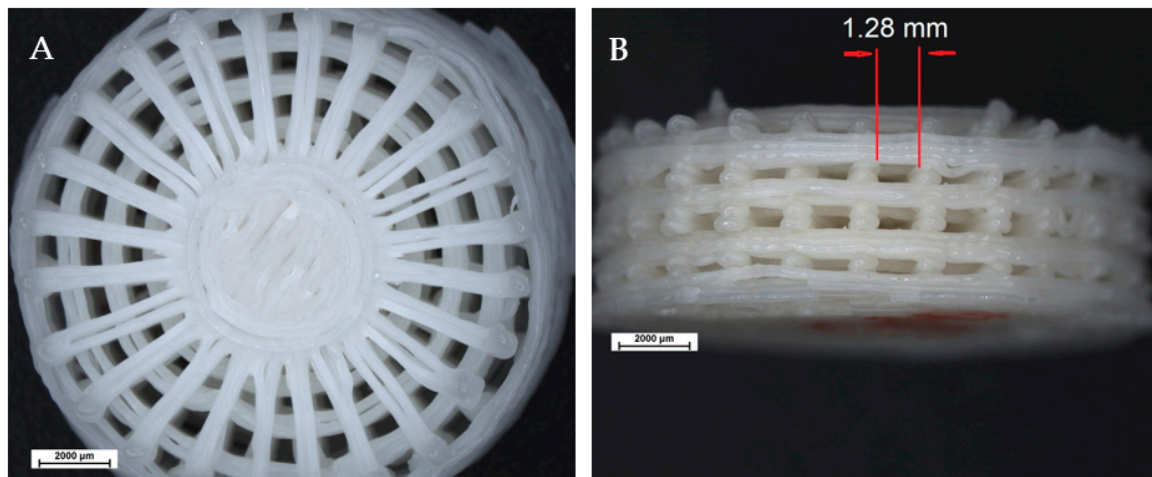
Figure 7. A representative bi-layer sample from the top (**A**) and side (**B**) views.

As listed in Table 2, the final open porosity of the bi-layer structures was 26.8 ± 2.6% on average measured by Archimedes' method. The solid parts were densified up to 96%TD (2.99 ± 0.01 g/cm^3). The open pores ranged from 605 ± 55 µm to 1.04 ± 0.031 mm measured for the largest edges of the trapezoids. These values demonstrate the extraordinary potentiality of the robocasting technique in fabricating porous structures with large tailored macroporosities which besides well densified strong solid parts, cannot be achieved by conventional ceramic manufacturing methods. Moreover, observation of the structure from the side view shows that during the printing of the outside ring the

filaments spanned the large gap between two radial supports equal to 1.28 mm without considerable deflection, proving the high strength and shape stability of the formulated paste in supporting its own and upper layers weights. This observation is noteworthy and can be the key parameter for printing more complex and stable structures with high accuracy.

Comprising two filaments next to each other, the average thickness of the rods was 619 ± 21 μm. Other physical characteristics of the sintered samples such as the diameters of the concentric rings and mean pores sizes are collected in Table 3. The pores sizes were considered equal to the diagonals of the trapezoids in the X-Y plane and the numbering under the pore sizes column presents their sequence from the core. Having the mean diameter of the dense core of 5.48 ± 0.11 mm and the overall diameter of the structure equal to 15.49 ± 0.35 mm, the dense core shared only 12.5% of the total volume of the structures.

Table 3. Measured diameters of the rings in the lattice part and pore sizes of the FGM bi-layer structures.

External Diameter (mm)					Mean Pore Size (μm)		
Core	1° ring	2° ring	3° ring	4° ring	1° ring	2° ring	3° ring
5.48 ± 0.11	7.92 ± 0.13	10.43 ± 0.15	13.02 ± 0.18	15.49 ± 0.35	605 ± 55	896 ± 52	1040 ± 31

3.1.5. Mechanical Properties

The representative stress-strain curves recorded during compression tests of the dense and lattice samples are depicted in Figure 8. Curves show that several cracks occurred before the final rupture of both samples. At the beginning of the loading, the resistance of the lattice samples against the external loading was attested by the increase of the applied stress as a function of samples' strains. After reaching an initial stress peak, a significant stress release occurred, which was recovered subsequently. Several stress release-recoveries led to further peaks inducing sawtooth-like curves. This phenomenon (repeated stress release-recovery) took place due to the failure of the different layers (load transfer). However, the final rupture occurred at maximum stress higher than the first peak. The dense samples, in the same way, firstly showed stress elevation up to an initial peak. Afterward, the samples managed to recover the released stress exhibiting an oscillating pattern at an almost narrow stress range, with a very moderate stress increase before the final failure.
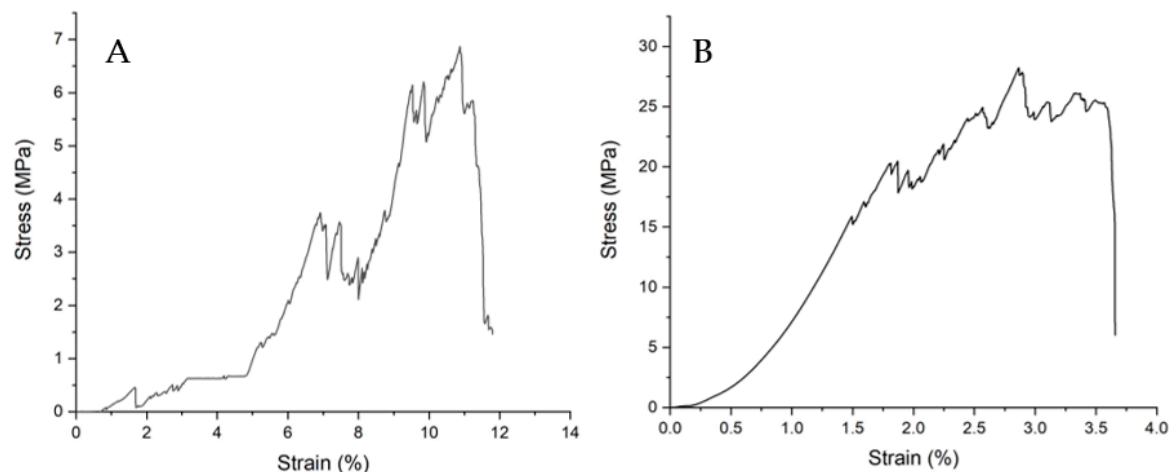
Figure 8. Registered stress-strain curves of the lattice (**A**) and dense samples (**B**), obtained during uniaxial compression tests.

The compressive strengths of the structures were found as 29 ± 4 MPa for the dense samples with an overall porosity of 13.9%, and 7 ± 4 MPa for the lattice structures with an overall porosity of 34.1%. This value for robocast HA lattices is reported in the ranges from 9 to 50 MPa with the porosity in the range from 26 to 71% [39,40,42,63] and for β-TCP ones is reported in the ranges from 11 to 20 MPa

with the porosity in the range from 27 to 40% [13,37,42]. The results obtained for the lattice structures in the current work are positioned in the lower limit of the literature data and were in the limit of the compressive strength of the cancellous bone which is reported in the range of 7–10 MPa [64].

The comparison of the mechanical properties of the dense samples with literature was not possible due to the lack of data. However, compared to the compressive strength of dense HA produced by the binder-jetting technique (equal to 22 MPa [65]), current results were significantly higher, suggesting the high potential of the robocasting technique in the production of well-densified parts. However, compared to the cortical bone with compression strength in the range of 130-180 MPa for the porosity in the range from 5 to 13% [2], the robocast dense samples had lower performance. In the future, mechanical properties could be improved by modifying the slicing procedure of the CAD design to credit higher overlapping between adjacent filaments and also by drying the samples in more controlled conditions [27,29].

3.1.6. Fracture Mechanism Analysis

Figure 9 shows the in-situ compression test configuration of the samples inside the ESEM, in which the stress was applied perpendicular to the ceramic filaments. The sample was held between two grips and the observations were done parallel to rods direction.
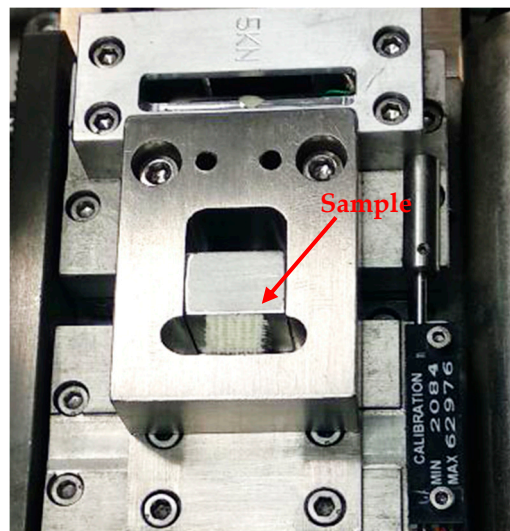
Figure 9. Test configuration as well as sample placement within the in-situ compression test device.

Figure 10 shows the condition of a sample after loading and the observation of a few sudden load drops. It can be seen that the failure mode consisted of longitudinal cracks aligned with the load axis running through the structure. Cracks were initiated from the external surface of the rods, nearby their intersections (image B). In fact, while loading, the area underneath two intersecting rods was under compression, while the perpendicular "free" rod fraction was probably submitted to flexural strength (with the upper parts in traction, as evidenced by the appearance of cracks indicated by white arrows in Figure 10). Increasing the loading increased the number of longitudinal cracks and the cracks propagated through the layered structure.
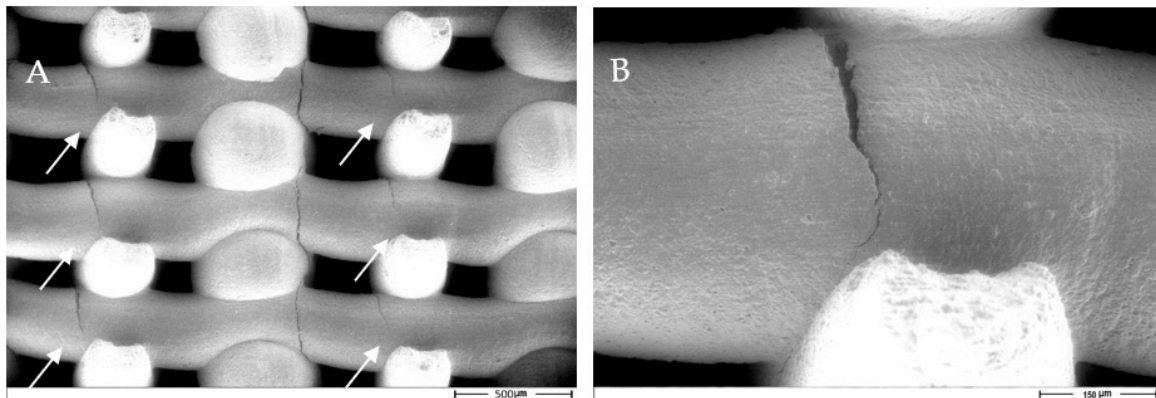
Figure 10. (**A**) Longitudinal cracks running through the structure of a porous scaffold during the compression test observed by ESEM, (**B**) a higher magnification image of a representative of the cracks.

It was observed that even after the development of several cracks, the structure preserved a certain mechanical resistance. This condition was revealed on stress-strain curves as the saw-tooth pattern (Figure 8A). Figure 11 shows the remaining parts of the lattice structure after the final fracture. It was reported that columnar structures that remain oriented along the load direction were responsible for such extended load-bearing capacity [40]. Of course, by load removal, these structures collapsed with no connection between the pillars able to provide any mechanical integrity.

Figure 11. Remaining columnar parts of a collapsed 3D porous structure within the in-situ compression test device.

Figure 12 illustrates the propagation of two parallel cracks during the compression test of the porous structure captured by ESEM. Image A shows two parallel cracks close to the intersection of the rods at the compressive loading of 2139 N. It can be seen that the cracks propagated with both inter (A) and intragranular (B) paths. Image B illustrates the condition of the cracks after increasing the applied loading to 2211 N. The dashed circle highlights the progression of the cracks' tip resulting in the crack's growth. However, because sample strain led to the redistribution of the applied force, the opposite sides of the previous cracks became closer. Image C shows the condition of the same cracks a few minutes after Image B, just before the final failure. Further growth of the cracks and bigger opening of the cracks' faces are visible. However, the final compressive loading dropped to 2083 N due to the stress relief by the cracks' growth.
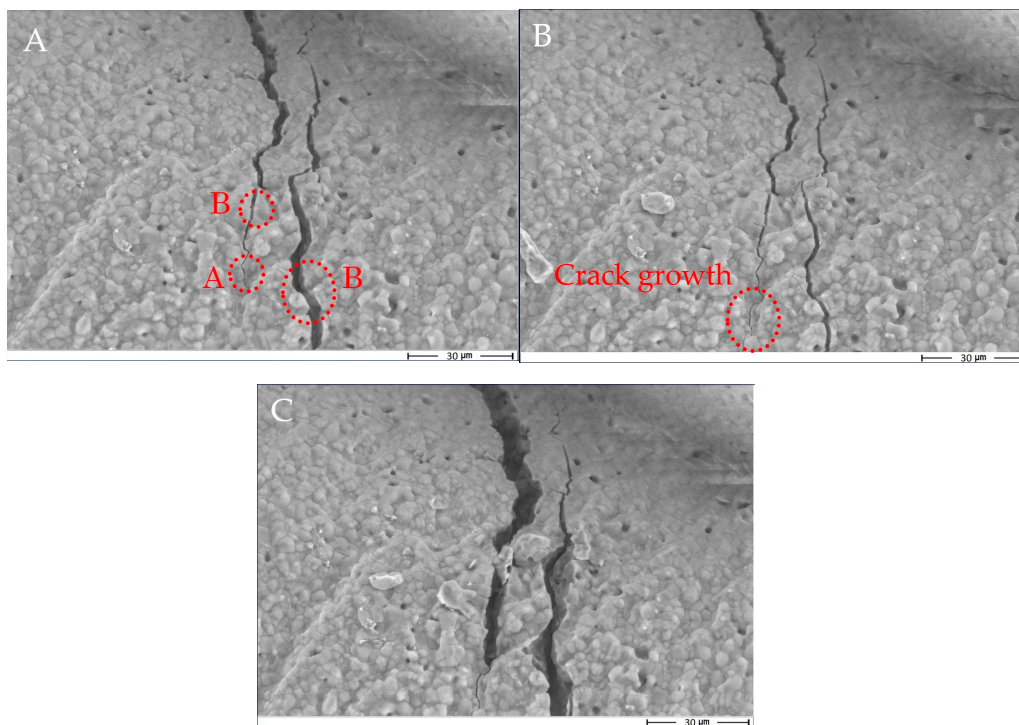
Figure 12. Cracks propagations through the microstructure of a porous sample under compressive loading taken by ESEM. (**A**) two parallel cracks propagated in opposite directions, (**B**) progression of the cracks tips by increasing the applied force, (**C**) condition of the cracks just before the final failure.

3.1.7. In Vitro Bioactivity Test

Figure 13 shows the SEM images obtained from a bi-layer sample after a preliminary bioactivity test. The newly deposited layer was observed on both dense and porous sections confirming in vitro bioactivity of the samples. However, as can be seen, in the dense sections (image A) some areas were not completely covered by the new layer. On the other hand, on the porous sections, entire filaments were covered by a newly formed thick layer (image B and C), suggesting higher bioactivity of the porous section compared to the dense one. The morphology of the deposited crystals was observed as rod-shaped or needle-like, in agreement with previous literature [60,61], and was distributed evenly on the surfaces (image D).

The chemical composition of the precipitated bioactivity layer was examined by EDS analysis. The results, collected in Table 4, suggested a calcium to phosphorous ratio of 1.33 for the precipitated layer, matching the Ca/P ratio of the octacalcium phosphate phase (OCP, $Ca_8H_2(PO4)_6.5H_2O$). Previous studies have shown that CaP phases such as OCP and dicalcium phosphate dihydrate (DCPD) are kinetically more preferred precipitation phases from supersaturated calcium and phosphorous solutions than HA. Indeed, from the thermodynamic point of view, HA is the most stable phase in SBF, but due to a substantially higher nucleation rate, OCP precipitates earlier than HA in physiological environments [66,67]. However, OCP is a precursor for the formation of nonstoichiometric biological apatites [68], which in longer times and by increasing the Ca/P ratio becomes more apatitic in nature and finally converts to HA. The stated phenomenon takes place according to the following reaction [65] and has been reported both for in vitro and in vivo tests [67–70].

$$5Ca_8H_2(PO_4)_6 \cdot 5H_2O \rightarrow 8Ca_5(PO_4)_3OH + 6H_3PO_4 + 17H_2O \tag{4}$$
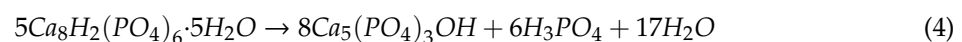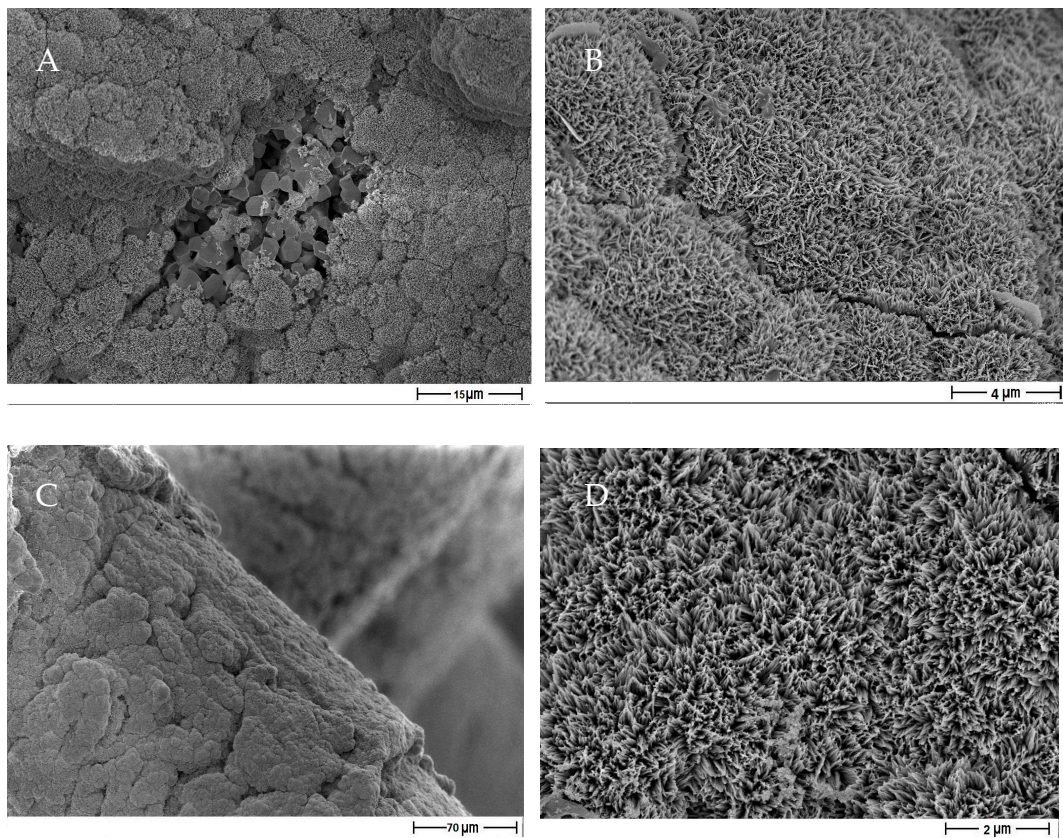
Figure 13. The new precipitated CaP layer on the surface of the bi-layer robocast structures. Low magnification images show the partial (**A**) and entire (**C**) coverage on the surface of dense and porous parts, respectively, and high magnification images show the evenly distributed rod-shaped crystals on the surface of the dense (**B**) and porous (**D**) parts.

**Table 4.** Chemical composition of the precipitated bioactivity layer, At%.

Ca	P	O	Si	Mg	Na	Ca/P
15.44	11.63	71.4	0.32	0.56	0.65	1.33

Therefore, it can be concluded that the precipitated CaP layer in this work was OCP which would have been transformed to HA if the bioactivity tests had been conducted for longer times.

3.2. Hybrid Technologies for Ceramic/Polymer Scaffolds

Figure 14 depicts some representative Ag^+-free and Ag^+-containing multi-layer ceramic/polymer scaffold fabricated by robocasting combined with the solvent casting/salt leaching method. Successful integration of these two technologies was achieved, in terms of a perfectly adherent external polymer/CaP layer to the inner bi-layer ceramic part. PCL is a biopolymer extensively used for controlled drug delivery providing uniform drug distribution and enabling long-term drug release up to several months [71].
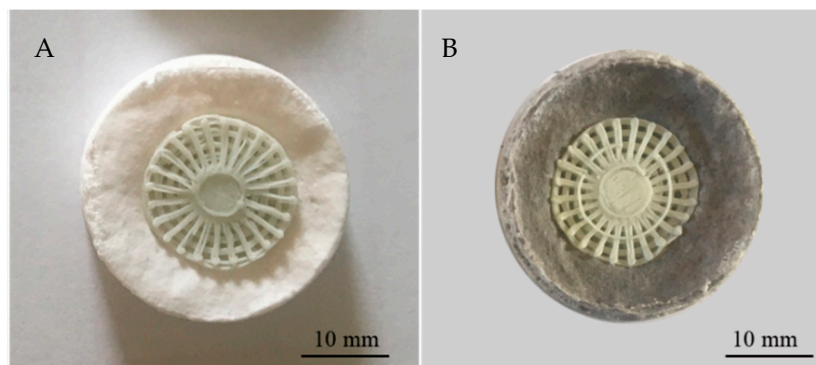
Figure 14. Digital photographs of two representative hybrid ceramic polymer samples. (**A**): Ag+-free PCL/BCP layer; (**B**): Ag$^+$-added PCL/BCP layer.

A mixture of HA and β-TCP phases (indicated as biphasic calcium phosphate, BCP) was added to the PCL solution (resulting in polymer/ceramic composite) to improve the osteoconductivity and bioactivity of the scaffold [72], while silver was added to impart the antimicrobial properties.

Figure 15 shows the microstructure of a representative PCL/BCP macroporous layer observed by SEM at two different magnifications. The left image illustrates the macroporosities left by NaCl after leaching out. The mean pore size was measured as 270 μm, marginally more than the mean NaCl granules sizes, while the geometric shape of the pores matches the morphology of the salt particles. The right image is a high magnification micrograph of the polymer strut, where we can observe CaP particles homogeneously distributed within the PCL matrix.
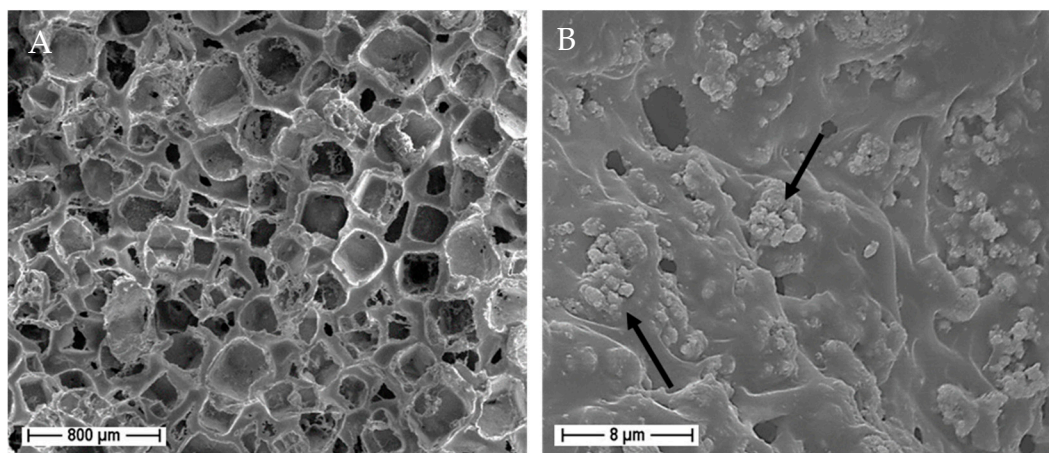
Figure 15. SEM micrographs of the PCL/BCP layer at two different low (**A**) and high (**B**) magnifications.

The antibacterial rate of the produced scaffolds was calculated using the following formula:

$$R = \frac{B - A}{B} \times 100\% \tag{5}$$

where *R*, *A* and *B* are the antibacterial rate, the average bacterial count of the sample (CFU) and the average bacterial count of the control sample (CFU), respectively.

Table 5 collects the results obtained from antibacterial tests. The Ag$^+$-free samples indicated as "control sample" showed a significant number of adhered bacteria in the order of 10^9 CFU/mL, suggesting a poor antimicrobial behavior of either the ceramic core and polymer layer. As expected, the number of adhered bacteria substantially decreased for the Ag$^+$ doped samples, showing the high effectiveness of the antibacterial layer to reduce the bacteria adhesion to the whole hybrid scaffold. The current results were slightly better than the average antibacterial results presented in the literature.

For example, Chen et al. [73] reported 90% improvement in the antibacterial properties of HA coating by doping 1 wt% of $AgNO_3$. However, it must be considered that although Ag has established antibacterial properties, it can be toxic if it is used in high concentrations. Therefore, a threshold value of the Ag percentage in the scaffold should be optimized considering both antimicrobial and cytotoxicity properties. Due to different Ag incorporation methods and different biological test methodologies, there is a discrepancy of the optimum concentrations in the literature. For example, Chen et al. [73] reported similar cell proliferation and differentiation for 1 wt% Ag-HA and HA. No significant cytotoxicity was reported for 2.05 wt% co-sputtered Ag-HA coating after incubation with human embryonic palatal mesenchymal cells for 24 h [74]. In another study, Karlov et al. [75] suggested a silver concentration of 7 wt% in coating as the optimum balance between antibacterial effect and minimum cytotoxicity.

Table 5. Antibacterial test results presenting bacterial count (CFU/mL) and antibacterial rate (%).

Sample Type	Ag-Doped Sample	Control Sample	R (%)
Adhered bacteria	$7.16 \times 10^4 \pm 3.5 \times 10^4$	$3.22 \times 10^9 \pm 3.07 \times 10^8$	100.00
Planktonic bacteria	$4.31 \times 10^4 \pm 1.70 \times 10^4$	$2.97 \times 10^9 \pm 3.82 \times 10^8$	100.00

Quantification of the planktonic bacteria, those present in the broth after 24 h incubation, was conducted to highlight the role of either the scaffold composition itself, to avoid toxic behavior, or the Ag^+ ions when released from the scaffold. Once again, the Ag^+-free control samples showed a high accumulation of planktonic bacteria (10^9 CFU/mL). This value was significantly decreased (10^4 CFU/mL) for the Ag^+-functionalized samples. Therefore, the results validated the release of antibacterial Ag^+ ions from the composite layer to the surrounding medium as an effective tool in eradicating the bacterial contamination of the surgery site.

Figures 16 and 17 show SEM micrographs of Ag^+-free and Ag^+-modified hybrid scaffolds, respectively. In Figure 16, the center image presents the overall structure of the sample, and the left and right images present the polymer and ceramic parts, respectively at higher magnifications. Biofilms made from bacterial colonization can be observed from the high magnification images on both polymer and ceramic parts, confirming a negligible role of both layers in preventing bacterial adhesion. On the contrary, Figure 17 shows the effectiveness of the Ag^+-functionalization since the microstructures were almost bacteria-free. Both the functionalized porous layer and ceramic parts were found free of bacteria. The absence of staphylococci also in the ceramic part (which does not contain Ag) suggests an effective Ag^+ release in the broth, as validated by the quantification of the planktonic bacteria.
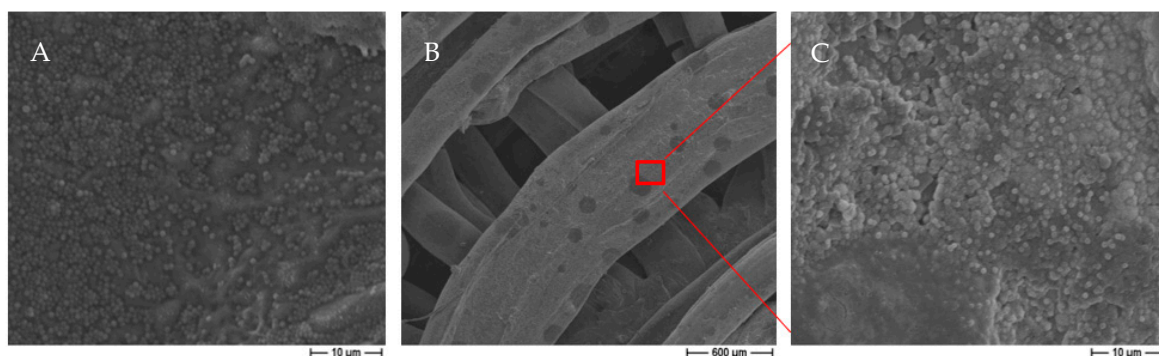
Figure 16. Micrographs of an Ag^+-free hybrid scaffold. (**A**,**C**) are high magnification of image (**B**): polymer (**A**) and ceramic (**C**) parts indicate bacterial biofilm on both surfaces.
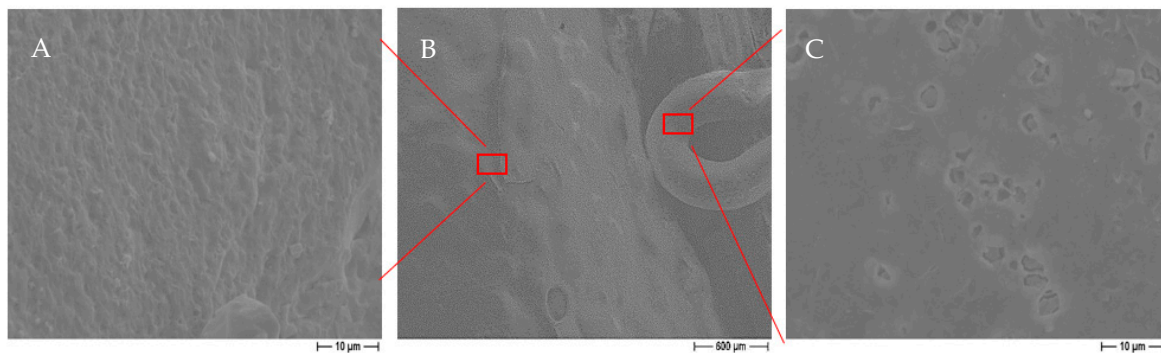
Figure 17. Micrographs of an Ag$^+$-functionalized hybrid scaffold. (**A**,**C**) are high magnification of image (**B**): polymer (**A**) and ceramic (**C**) parts indicate clean bacterial free surfaces.

4. Conclusions

Robocasting was successfully used for the production of dense, porous and bi-layer (FGM) hydroxyapatite structures. The bi-layer structure was composed of a dense core surrounded by a lattice part, fabricated in a single printing step. To the best of our knowledge, it was the first time that such a complex part, made by integrating monolithic and porous structures, was fabricated by the robocasting technique.

While the dense structure showed some large flaws and consequently a moderate compressive strength, even if higher to structures made by binder-jetting, the produced lattice structure fulfilled all biological and mechanical criteria for the non-load-bearing biomedical applications. The osteoconductive properties of the bi-layer parts were verified by soaking the sintered samples in SBF, which showed good in vitro bioactivity, especially the porous parts: the precipitated layer was OCP which is believed to be a precursor of biological HA.

As an innovation, a new PCL/CaP composite macroporous layer was also added to the already fabricated FGM structures to introduce more functionality e.g., antibacterial properties. This third hybrid layer combined the advantages of high biological properties of CaP component and effective drug entrapment in the polymeric part. The result was FGM tri-layer samples in which each layer had special functions: loadbearing for the dense core layer, osteoconductivity and osteoinductivity for the intermediate porous layer, and antibacterial and drug delivery for the outer composite layer. Antibacterial tests showed that the hybrid structure was effective in releasing antibacterial Ag$^+$ ions to the surrounding medium and showed its potential efficiency in limiting *Staphylococcus aureus* proliferation during surgery. As a final note, this hybrid material can be considered as a model system to pave the way towards new multifunctional biomaterials for tissue engineering applications.

References

1. Sultana, N. *Biodegradable Polymer-Based Scaffolds for Bone Tissue Engineering*; Springer: Berlin/Heidelberg, Germany; New York, NY, USA; Dordrecht, The Netherlands; London, UK, 2013. [CrossRef]

2. Liu, H. *Nanocomposites for Musculoskeletal Tissue Regeneration*; Woodhead Publishing: Kidlington, UK, 2016.

3. Brown, O.; McAfee, M.; Clarke, S.; Buchanan, F. Sintering of biphasic calcium phosphates. *J. Mater. Sci. Mater. Med.* **2010**, *21*, 2271–2279. [CrossRef] [PubMed]

4. LeGeros, R.Z. Properties of osteoconductive biomaterials: Calcium phosphates. *Clin. Orthop. Relat. Res.* **2002**, *395*, 81–98. [CrossRef] [PubMed]

5. Hench, L.L. *An Introduction to Bioceramics*, 2nd ed.; Imperial College Press: London, UK, 2013.

6. Dorozhkin, S.V. Bioceramics of calcium orthophosphates. *Biomaterials* **2010**, *31*, 1465–1485. [CrossRef] [PubMed]

7. Hwa, L.C.; Rajoo, S.; Mohd Noor, A.; Norhayati, A.; Uday, M. Recent advances in 3D printing of porous ceramics: A review. *Curr. Opin. Solid State Mater. Sci.* **2017**, *21*, 323–347. [CrossRef]

8. Gauthier, O.; Bouler, J.M.; Aguado, E.; Pilet, P. Macroporous biphasic calcium phosphate ceramics: Influence of macropore diameter and macroporosity percentage on bone ingrowth. *Biomaterials* **1998**, *19*, 133–139. [CrossRef]

9. Schephake, H.; Neukam, E.W.; Klosa, D. Influence of pore dimensions on bone ingrowth into porous hydroxylapatite blocks used as bone graft substitutes: A histometric study. *Int. J. Oral Maxillofac. Surg.* **1991**, *20*, 53–58. [CrossRef]

10. Samavedi, S.; Whittington, A.R.; Goldstein, A.S. Calcium phosphate ceramics in bone tissue engineering: A review of properties and their influence on cell behavior. *Acta Biomater.* **2013**, *9*, 8037–8045. [CrossRef]

11. Dorozhkin, S.V. Calcium orthophosphate bioceramics. *Ceram. Int.* **2015**, *41*, 13913–13966. [CrossRef]

12. Cyster, L.; Grant, D.; Howdle, S.; Rose, F.; Irvine, D.; Freeman, D.; Scotchford, C.; Shakesheff, K. The influence of dispersant concentration on the pore morphology of hydroxyapatite ceramics for bone tissue engineering. *Biomaterials* **2005**, *26*, 697–702. [CrossRef]

13. Tarafder, S.; Balla, V.K.; Davies, N.M.; Bandyopadhyay, A.; Bose, S. Microwave-sintered 3D printed tricalcium phosphate scaffolds for bone tissue engineering. *J. Tissue Eng. Regen. Med.* **2013**, *7*, 631–641. [CrossRef]

14. Zhang, C.; Chen, F.; Huang, Z.; Jia, M.; Chen, G.; Ye, Y.; Lin, Y.; Liu, W.; Chen, B.; Shen, Q.; et al. Additive manufacturing of functionally graded materials: A review. *Mater. Sci. Eng. A* **2019**, *764*, 138209. [CrossRef]

15. Lee, H.; Jang, T.S.; Song, J.; Kim, H.E.; Jung, H.D. The production of porous hydroxyapatite scaffolds with graded porosity by sequential freeze-casting. *Materials* **2017**, *10*, 367. [CrossRef] [PubMed]

16. Fu, Q.; Rahaman, M.N.; Dogan, F.; Ba, B.S. Freeze-cast hydroxyapatite scaffolds for bone tissue engineering applications. *Biomed. Mater.* **2008**, *3*. [CrossRef] [PubMed]

17. Wang, Q.; Wang, Q.; Wang, C. Preparation and evaluation of a biomimetic scaffold with porosity gradients in vitro. *An. Acad. Bras. Ciênc.* **2012**, *84*, 9–16. [CrossRef] [PubMed]

18. Chamary, S.; Hautcoeur, D.; Hornez, J.C.; Leriche, A.; Cambier, F. Bio-inspired hydroxyapatite dual core-shell structure for bone substitutes. *J. Eur. Ceram. Soc.* **2017**, *37*, 5321–5327. [CrossRef]

19. Pompe, W.; Worch, H.; Epple, M.; Friess, W.; Gelinsky, M.; Greil, P.; Hempele, U.; Scharnweber, D.; Schulte, K. Functionally graded materials for biomedical applications. *Mater. Sci. Eng. A* **2003**, *362*, 40–60. [CrossRef]

20. Macchetta, A.; Turner, I.G.; Bowen, C.R. Fabrication of HA/TCP scaffolds with a graded and porous structure using a camphene-based freeze-casting method. *Acta Biomater.* **2009**, *5*, 1319–1327. [CrossRef]

21. Sanchez-Salcedo, S.; Werner, J.; Vallet-Regi, M. Hierarchical pore structure of calcium phosphate scaffolds by a combination of gel-casting and multiple tape-casting methods. *Acta Biomater.* **2008**, *4*, 913–922. [CrossRef]

22. Petit, C.; Tulliani, J.M.; Tadier, S.; Meille, S.; Chevalier, J.; Palmero, P. Novel calcium phosphate/PCL graded samples: Design and development in view of biomedical applications. *Mater. Sci. Eng. C* **2019**, *97*, 336–346. [CrossRef]

23. Lewis, J.A.; Gratson, G.M. Direct writing in three dimensions. *Mater. Today* **2004**, *7*, 32–39. [CrossRef]

24. Fu, Z.; Freihart, M.; Wahl, L.; Tobias Fey, T.; Greil, P.; Travitzky, N. Micro- and macroscopic design of alumina ceramics by robocasting. *J. Eur. Ceram. Soc.* **2017**, *37*, 3115–3124. [CrossRef]

25. Marchi, C.S.; Kouzeli, M.; Rao, R.; Lewis, J.; Dunand, D. Alumina–aluminum interpenetrating-phase composites with three-dimensional periodic architecture. *Scr. Mater.* **2003**, *49*, 861–866. [CrossRef]

26. Stanciuc, A.M.; Sprecher, C.M.; Adrien, J.; Roiban, L.I.; Alini, M.; Gremillard, L.; Peroglio, M. Robocast zirconia-toughened alumina scaffolds: Processing, structural characterisation and interaction with human primary osteoblasts. *J. Eur. Ceram. Soc.* **2018**, *18*, 845–853. [CrossRef]

27. Feilden, E.; García-Tunón Blanca, E.; Giuliani, F.; Saiz, E.; Vandeperre, L. Robocasting of structural ceramic parts with hydrogel inks. *J. Eur. Ceram. Soc.* **2016**, *36*, 2525–2533. [CrossRef]

28. Wahl, L.; Lorenz, M.; Biggemann, J.; Travitzky, N. Robocasting of reaction bonded silicon carbide structures. *J. Eur. Ceram. Soc.* **2019**, *39*, 4520–4526. [CrossRef]

29. Eqtesadi, S.; Motealleh, A.; Miranda, P.; Lemos, A.; Rebelo, A.; Ferreira, J.M. A simple recipe for direct writing complex 45S5 Bioglasss 3D scaffolds. *Mater. Lett.* **2013**, *93*, 68–71. [CrossRef]

30. Fu, Q.; Saiz, E.; Tomsia, A.P. Direct ink writing of highly porous and strong glass scaffolds for load-bearing bone defects repair and regeneration. *Acta Biomater.* **2011**, *7*, 3547–3554. [CrossRef]

31. Barberi, J.; Nommeots-Nomm, A.; Fiume, E.; Verne, E.; Massera, J.; Baino, F. Mechanical characterization of pore-graded bioactive glass scaffolds produced by robocasting. *Biomed. Glas.* **2019**, *5*, 140–147. [CrossRef]

32. Smay, J.E.; Nadkarni, S.S.; Xu, J. Direct writing of dielectric ceramics and base metal electrodes. *Int. J. Appl. Ceram. Technol.* **2007**, *4*, 47–52. [CrossRef]

33. Maroulakos, M.; Kamperos, G.; Tayebi, L.; Halazonetis, D.; Ren, Y. Applications of 3D printing on craniofacial bone repair: A systematic review. *J. Dent.* **2019**, *80*, 1–14. [CrossRef]

34. Zocca, A.; Colombo, P.; Gomes, C.M.; Gunster, J. Additive Manufacturing of Ceramics: Issues, Potentialities, and Opportunities. *J. Am. Ceram. Soc.* **2015**, *98*, 1983–2001. [CrossRef]

35. Michna, S.; Wu, W.; Lewis, J.A. Concentrated hydroxyapatite inks for direct-write assembly of 3-D periodic scaffolds. *Biomaterials* **2005**, *26*, 5632–5639. [CrossRef] [PubMed]

36. Miranda, P.; Pajares, A.; Saiz, E.; Tomsia, A.P.; Guiberteau, F. Mechanical properties of calcium phosphate scaffolds fabricated by robocasting. *J. Biomed. Mater. Res. A* **2008**, *85*, 218–227. [CrossRef] [PubMed]

37. Martínez-Vázquez, F.J.; Perera, F.H.; Miranda, P.; Pajares, A.; Guiberteau, F. Improving the compressive strength of bioceramic robocast scaffolds by polymer infiltration. *Acta Biomater.* **2010**, *6*, 4361–4368. [CrossRef] [PubMed]

38. Franco, J.; Hunger, P.; Launey, M.; Tomsia, A.; Saiz, E. Direct write assembly of calcium phosphate scaffolds using a water-based hydrogel. *Acta Biomater.* **2010**, *6*, 218–228. [CrossRef]

39. Paredes, C.; Martínez-Vázquez, F.J.; Pajares, A.; Miranda, P. Development by robocasting and mechanical characterization of hybrid HA/PCL coaxial scaffolds for biomedical applications. *J. Eur. Ceram. Soc.* **2019**, *39*, 4375–4383. [CrossRef]

40. Roleček, J.; Pejchalová, L.; Martínez-Vázquez, F.; Miranda González, P.; Salamon, D. Bioceramic scaffolds fabrication: Indirect 3D printing combined with ice templating vs. robocasting. *J. Eur. Ceram. Soc.* **2019**, *39*, 1595–1602. [CrossRef]

41. Cesarano, J., III; Dellinger, J.G.; Saavedra, M.P.; Gill, D.D. Customization of load-bearing hydroxyapatite lattice scaffolds. *Int. J. Appl. Ceram. Technol.* **2005**, *2*, 212–220. [CrossRef]

42. Miranda, P.; Pajares, A.; Saiz, E.; Tomsia, A.; Guiberteau, F. Fracture modes under uniaxial compression in hydroxyapatite scaffolds fabricated by robocasting. *J. Biomed. Mater. Res. A* **2007**, *83*, 646–657. [CrossRef]

43. Martinez-Vazquez, F.J.; Perera, F.H.; Meulen, I.V.D.; Heise, A.; Pajares, A.; Miranda, P. Impregnation of b-tricalcium phosphate robocast scaffolds by in situ polymerization. *J. Biomed. Mater. Res. A* **2013**, *101*, 3086–3096. [CrossRef]

44. Sorrentino, R.; Cochis, A.; Azzimonti, B.; Caravaca, C.; Chevalier, J.; Kuntz, M.; Porporati, A.A.; Streicher, R.M.; Rimondini, L. Reduced bacterial adhesion on ceramics used for arthroplasty applications. *J. Eur. Ceram. Soc.* **2018**, *38*, 963–970. [CrossRef]

45. Ou, S.F.; Chung, R.J.; Lin, L.H.; Chiang, Y.C.; Huang, C.F.; Ou, K.L. A mechanistic study on the antibacterial behavior of silver doped bioceramic. *J. Alloys Compd.* **2015**, *629*, 362–367. [CrossRef]

46. Yang, S.; Zhang, Y.; Yu, J.; Zhen, Z.; Huang, T.; Tang, Q.; Chu, P.K.; Qi, L.; Hongbo, L. Antibacterial and mechanical properties of honeycomb ceramic materials incorporated with silver and zinc. *Mater. Des.* **2014**, *59*, 461–465. [CrossRef]

47. Balamurugan, A.; Balossier, G.; Laurent-Maquin, D.; Pina, S.; Rebelo, A.; Faure, J.; Ferreira, J. An in vitro biological and anti-bacterial study on a sol–gel derived silver-incorporated bioglass system. *Dent. Mater.* **2008**, *24*, 1343–1351. [CrossRef] [PubMed]

48. Mohammadi, M.; Tulliani, J.M.; Palmero, P. Fabrication of dense and porous biphasic calcium phosphates: Effect of dispersion on sinterability and microstructural development. *Int. J. Appl. Ceram. Technol.* **2019**, *16*, 1797–1806. [CrossRef]

49. ISO 10545-3. *Ceramic tiles—Part 3: Determination of Water Absorption, Apparent Porosity, Apparent Relative Density and Bulk Density*; International Organization for Standardization: Geneva, Switzerland, 2018.

50. ASTM C773-88. *Standard Test Method for Compressive (Crushing) Strength of Fired Whiteware Materials*; American Society for Testing and Materials: West Conshohocken, PE, USA, 2016.

51. Marcassoli, P.; Cabrini, M.; Tirillò, J.; Bartuli, C.; Palmero, P.; Montanaro, L. Mechanical Characterization of Hydroxiapatite Micro/Macro-Porous Ceramics Obtained by Means of Innovative Gel-Casting Process. *Key Eng. Mater.* **2009**, *417*, 565–568. [CrossRef]

52. Benaqqa, C.; Chevalier, J.; Saädaoui, M.; Fantozzi, G. Slow crack growth behaviour of hydroxyapatite ceramics. *Biomaterials* **2005**, *26*, 6106–6112. [CrossRef]

53. Palmero, P.; Fantozzi, G.; Lomello, F.; Bonnefont, G.; Montanaro, L. Creep behaviour of alumina/YAG composites prepared by different sintering routes. *Ceram. Int.* **2012**, *38*, 433–441. [CrossRef]

54. ISO 23317. *Ceramic Tiles—Part 3: Implants for Surgery—In Vitro Evaluation for Apatite-Forming Ability of Implant Materials*; International Organization for Standardization: Geneva, Switzerland, 2014.

55. Afghah, F.; Ullah, M.; Seyyed Monfared Zanjani, J.; Akkus Sut, P.; Sen, O.; Emanet, M.; Saner Okan, B.; Culha, M.; Menceloglu, M.; Yildiz, M.; et al. 3D printing of silver-doped polycaprolactone-poly(propylene succinate) composite scaffolds for skin tissue engineering. *Biomed. Mater.* **2020**, 15. [CrossRef]

56. Banche, G.; Allizond, V.; Bracco, P.; Bistolfi, A.; Boffano, M.; Cimino, A.; Brach Del Prever, E.M.; Cuffini, A.M. Interplay between surface properties of standard, vitamin E blended and oxidised ultra high molecular weight polyethylene used in total joint replacement and adhesion of Staphylococcus aureus and Escherichia coli. *Bone Jt. J.* **2014**, *96*, 497–501. [CrossRef]

57. Cazzola, M.; Ferraris, S.; Allizond, V.; Bertea, C.M.; Novara, C.; Cochis, A.; Geobaldo, F.; Bistolfi, A.; Cuffini, A.M.; Rimondini, L.; et al. Grafting of peppermint essential oil to chemically treated Ti6Al4V alloy to counteract bacterial adhesion. *Surf. Coat. Technol.* **2019**, *378*, 125011. [CrossRef]

58. Ferraris, S.; Spriano, S.; Miola, M.; Bertone, E.; Allizond, V.; Cuffini, A.M.; Banche, G. Bioactive and antibacterial titanium surfaces through a modified oxide layer and embedded silver nanoparticles: Effect of reducing/stabilizing agents on precipitation and properties of the nanoparticles. *Surf. Coat. Technol.* **2018**, *344*, 177–189. [CrossRef]

59. Banche, G.; Bracco, P.; Allizond, V.; Bistolfi, A.; Boffano, M.; Cimino, A.; Brach Del Prever, E.M.; Cuffini, A.M. Do crosslinking and vitamin E stabilization influence microbial adhesions on UHMWPE-based biomaterials? *Clin. Orthop. Relat. Res.* **2015**, *473*, 974–986. [CrossRef]

60. Rahaman, M.N. *Ceramic Processing*, 2nd ed.; CRC Press: Boca Raton, FL, USA, 2017. [CrossRef]

61. Potoczek, M.; Zima, A.; Paszkiewicz, Z.; Slosarczyk, A. Manufacturing of highly porous calcium phosphate bioceramics via gel-casting using agarose. *Ceram. Int.* **2009**, *35*, 2249–2254. [CrossRef]

62. Roopavath, U.K.; Malferrari, S.; Van Haver, A.; Verstreken, A.; Narayan Rath, S.; Kalaskar, D.M. Optimization of extrusion based ceramic 3D printing process for complex bony design. *Mater. Des.* **2019**, *162*, 263–270. [CrossRef]

63. Martınez-Vazquez, F.; Pajares, A.; Miranda, P. Effect of the drying process on the compressive strength and cell proliferation of hydroxyapatite-derived scaffolds. *Int. J. Appl. Ceram. Technol.* **2017**, *14*, 1101–1106. [CrossRef]

64. Palmero, P. Ceramic–polymer Nanocomposites for Bone-Tissue Regenerarion. In *Nanocomposites for Musculoskeletal Tissue Regeneration*; Woodhead Publishing: Duxford, UK, 2016; pp. 331–367.

65. Seitz, H.; Rieder, W.; Irsen, S.; Leukers, B.; Tille, C. Three-dimensional printing of porous ceramic scaffolds for bone tissue engineering. *J. Biomed. Mater. Res. B* **2005**, *74*, 782–788. [CrossRef]

66. Xin, R.; Leng, Y.; Chen, J.; Zhang, Q. A comparative study of calcium phosphate formation on bioceramics in vitro and in vivo. *Biomaterials* **2005**, *26*, 6477–6486. [CrossRef]

67. Lu, X.; Leng, Y. Theoretical analysis of calcium phosphate precipitation in simulated body fluid. *Biomaterials* **2005**, *26*, 1097–1108. [CrossRef]

68. Eidelman, N.; Chow, L.C.; Brown, W.E. Calcium phosphate saturation levels in ultrafiltered serum. *Calcif. Tiss. Int.* **1987**, *40*, 71–78. [CrossRef]

69. Leeuwenburgh, S.C.; Wolke, J.G.; Siebers, M.C.; Schoonman, J.; Jansen, J.A. In vitro and in vivo reactivity of porous, electrosprayed calcium phosphate coatings. *Biomaterials* **2006**, *27*, 3368–3378. [CrossRef]

70. Leng, Y.; Chen, J.; Qu, S. TEM study of calcium phosphate precipitation on HA/TCP ceramics. *Biomaterials* **2003**, *24*, 2125–2131. [CrossRef]

71. Poh, P.S.; Hutmacher, D.W.; Holzapfel, B.M.; Solanki, A.K.; Stevens, M.M.; Woodruff, M.A. In vitro and in vivo bone formation potential of surface calcium phosphate-coated polycaprolactone and polycaprolactone/bioactive glass composite scaffolds. *Acta Biomater.* **2016**, *30*, 319–333. [CrossRef]

72. Dziadek, M.; Stodolak-Zych, E.; Cholewa-Kowalska, K. Biodegradable ceramic-polymer composites for biomedical applications: A review. *Mater. Sci. Eng. C* **2017**, *71*, 1175–1191. [CrossRef]

73. Chen, W.; Oh, S.; Ong, A.; Oh, N.; Liu, Y.; Courtney, H.; Appleford, M.; Ong, J. Antibacterial and osteogenic properties of silver-containing hydroxyapatite coatings produced using a sol gel process. *J. Biomed. Mater. Res.* **2007**, *82A*, 899–906. [CrossRef]

74. Chen, W.; Liu, Y.; Courtney, H.; Bettenga, M.; Agrawal, C.; Bumgardner, J.; Ong, J. In vitro anti-bacterial and biological properties of magnetron co-sputtered silver-containing hydroxyapatite coating. *Biomaterials* **2006**, *27*, 5512–5517. [CrossRef]

75. Karlov, A.; Shakhov, V.; Kolobov, J. Definition of silver concentration in calcium phophate coatings on titanium implants ensuring balancing of bactericidity and cytotoxicity. *Key Eng. Mater.* **2000**, *192*, 207–210. [CrossRef]